ICARUS **66**, 297–323 (1986)

Satellite "Wakes" and the Orbit of the Encke Gap Moonlet

MARK R. SHOWALTER[1]

Cornell University, Ithaca, New York 14853

JEFFREY N. CUZZI

NASA/Ames Research Center, Moffett Field, California 94035

ESSAM A. MAROUF

Stanford University, Stanford, California 94305

AND

LARRY W. ESPOSITO

University of Colorado, Boulder, Colorado 80309

Received October 17, 1985; revised January 22, 1986

Quasiperiodic optical depth variations have been observed in the Voyager stellar (PPS) and radio occultation profiles near the Encke Gap of Saturn's rings, and have also been detected in one Voyager image. These fluctuations are believed to be the gravitational "wakes" of a moonlet orbiting within the gap. The existence of such a body had already been proposed by J. N. Cuzzi and J. D. Scargle (1985, *Astrophys. J.* **292,** 276–290), based on radial "wavy edges" visible in numerous Voyager images of the gap. We develop a general model for these wakes, and use the results to estimate the moonlet's orbit and mass from the occultation data; this model may have broader applications to planetary rings. The moonlet longitude is best determined from the PPS scan interior to the gap, and is estimated to trail the observed profile by 32°. Considering the uncertainty caused by our neglect of particle collisions and self-gravity, the longitude is consistent with other estimates obtained from a second portion of the PPS scan exterior to the gap, and also from the radio profile. The moonlet orbits close to the center of the gap at an estimated semimajor axis of 133,603 ± 10 km; it has a mass of $5\text{–}10 \times 10^{-12}$ Saturn masses, which corresponds to a radius of ~ 10 km if it is composed primarily of water ice. The consistency of the orbit parameters inferred from the PPS, radio, and wavy edge data virtually guarantees that a single dominant moonlet orbits within the gap. © 1986 Academic Press, Inc.

1. INTRODUCTION

The Encke Gap, located in the outer third of Saturn's A Ring (centered near radius 133,600 km and of width 325 km) is one of several gaps which are not associated with any known satellite resonance. Therefore, the process which resists the natural tendency of ring material to close the gap by diffusion has been a major puzzle. The Encke Gap does contain two or more narrow, discontinuous ringlets which appear kinked and/or clumpy in the Voyager images, with morphology and particle size reminiscent of Saturn's F Ring (Smith *et al.*, 1981, 1982). Evidence for additional fragmental material in the gap is found in the Voyager stellar occultation observations (Lane *et al.*, 1982). The F Ring's peculiar structure has been widely attributed to the gravitational perturbations from its two adjacent "shepherding" satellites, Pandora and Prometheus (Dermott, 1981;

---

[1] Currently NRC Associate, NASA/Ames Research Center.

0019-1035/86 $3.00

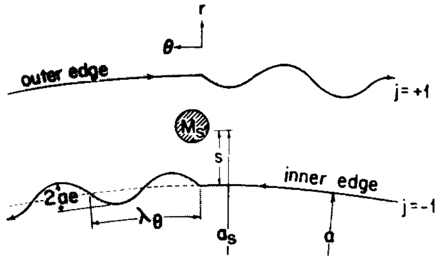

FIG. 1.1. The ring–moonlet interaction, as viewed in the rotating frame of the moonlet. Each particle receives a gravitational "kick" as it drifts past the moonlet, and subsequently proceeds on a sinusoidal (eccentric) path. The overall direction of rotation is toward the left. In this and successive sketches, the radial scale is greatly expanded; the true ratio of λ_θ to s is roughly 3π.

Showalter and Burns, 1982). The similarity of the Encke ringlets led to a suspicion that one or more moonlets might be embedded within the gap, which could produce the observed ringlet structure and also keep the gap clear by their gravitational torques (cf. Lissauer *et al.*, 1981; Hénon 1981, 1983).

Stronger, but still indirect, evidence for embedded satellites was presented by Cuzzi and Scargle (1985; hereafter CS), who demonstrated that the location and morphology of certain smooth radial undulations along the gap edges could be understood if a single dominant moonlet of about 10 km radius is orbiting within the gap. The situation and relevant physics, which were originally developed in the galactic context by Julian and Toomre (1966), were reviewed by Cuzzi *et al.* (1984); below we briefly outline the nature of the moonlet–ring interaction.

As viewed from a moonlet at semimajor axis[2] a_s within a gap, ring material at nearby semimajor axis a slowly drifts past due to the gradient of the Keplerian angular velocity $\omega(a)$. During its brief passage a ring particle feels a net gravitational acceleration, which integrates to a small radial component of velocity v_r toward the moonlet at the end of the "encounter." Once it has passed, the ring particle proceeds on a Keplerian orbit, which it maintains without any further influence from the moonlet until one synodic period (many orbital periods) later. Its new radial velocity translates to a small orbital eccentricity, and it reaches its first radial extremum (apocenter or pericenter, depending on the direction of v_r) one quarter period after the encounter. The ring material drifts relative to the moonlet at a rate

$$v_{\rm rel} = a\frac{d\omega}{da}s \approx -\frac{3}{2}\omega(a)s, \qquad (1.1)$$

where $s \equiv a - a_s$. This causes successive radial extrema to be spaced evenly by the azimuthal wavelength

$$\lambda_\theta(a) = \frac{2\pi}{\omega(a)}|v_{\rm rel}(a)| \approx 3\pi|s|. \qquad (1.2)$$

This pattern leads the satellite on the gap's inner edge and trails it on the outer edge, due to the sense of the relative velocity of ring material (see Fig. 1.1). The measured azimuthal wavelengths of CS (~1500 km on both edges) are consistent with a satellite orbiting near the center of the 325-km-wide gap.

The amplitude of the induced radial oscillations may be roughly estimated as follows. The ring particle experiences a radial acceleration $\dot{v}_r \sim GM_s/s^2$, where M_s is the satellite mass, during the brief encounter time interval $t_{\rm enc} \sim |s/v_{\rm rel}| \sim 1/\omega$. The net radial velocity $v_r \sim \dot{v}_r t_{\rm enc}$ corresponds to an eccentricity $e \sim |v_r|/a\omega$. Combining these expressions yields

$$e \sim \frac{|\dot{v}_r|}{a\omega^2} \sim \frac{M_s}{M_p}\left(\frac{a}{a - a_s}\right)^2, \qquad (1.3)$$

where M_p is the central planetary mass. When the eccentricity is evaluated within a formal three-body analysis, the result is the same expression as (1.3) above, except for

---

[2] In this paper, the term "semimajor axis" will always refer to the radius of the guiding center of a body's motion. It will not refer to the osculating orbital element, which differs from the above definition by $O(J_2)$ (cf. Greenberg, 1981).

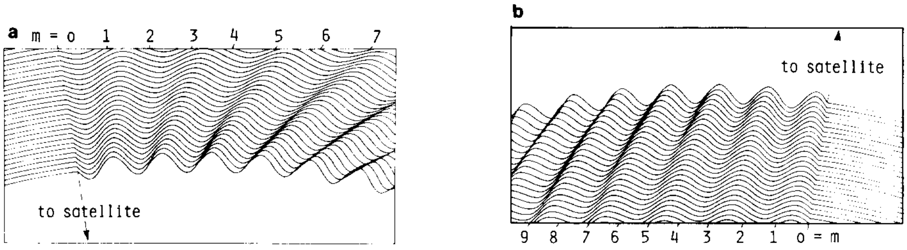

FIG. 1.2. A sketch of a moonlet wake, showing a number of its qualitative properties, at the outer (a) and inner (b) edges of a gap. The curves describe trajectories in the rotating frame for ring particles with uniformly spaced semimajor axes. The radial oscillations show increasing wavelength and decreasing amplitude with radial distance from the moonlet. Particles begin their oscillations in phase, but the varying wavelength causes trajectories to pile up some distance "downstream." Successive density crests and troughs are numbered by the extremum index *m* (see Sect. 2.2). The outermost streamlines begin to intersect within the figure; collisions will modify the pattern beyond this point. Note that, if it were not for the large radial expansion of this sketch, the density features would be very nearly azimuthal.

a multiplicative factor of 2.24 (Julian and Toomre, 1966). The ~2-km radial amplitudes measured by CS indicate that the Encke Gap satellite is ~10 km in radius, based on a density of 1 g/cm^3.

Of course, the perturbations of such a moonlet are not only felt by material at the gap edge, but also by ring material over a range of neighboring orbital radii. The resultant radial oscillations do, however, vary in amplitude ae and wavelength λ_θ due to the increasing distance $|s|$ of the ring material from the moonlet. This fact has little observable consequence near the satellite, because the induced oscillations are nearly in phase, and hence the surface density of material is undisturbed. However, since λ_θ is proportional to s, neighboring streamlines gradually go out of phase. The distance between neighboring streamlines begins to vary, resulting in a periodic variation in surface density (see Figs. 1.2a and b). Eventually, a point is reached where neighboring streamlines formally intersect, and the pattern is expected to damp out soon thereafter.

Despite its wavelike appearance, this pattern differs in important ways from other density features in Saturn's rings. It is driven entirely by the satellite; no interactions between ring particles are required. Thus, unlike the well-known spiral density and bending waves, this pattern's existence does not depend on the mass density and particle collision rate in the rings. In this sense, it is not a wave at all. To emphasize this distinction, we will refer to this phenomenon as a moonlet "wake," by analogy to the localized disturbance trailing, and fixed in the frame of, a motorboat.

By observing the occultation of the star δ Scorpii by Saturn's rings, the Voyager 2 photopolarimeter experiment (PPS) obtained a complete radial profile of ring optical depth sampled every 100 m (Lane *et al.*, 1982). Immediately interior to the Encke Gap, it detected a regular pattern of optical depth fluctuations. The pattern has a wavelength which systematically increases from ~5 km near the gap edge to ~20 km at a distance 200 km inward from the edge, while the amplitude decreases monotonically; beyond this point, the fluctuations are masked by noise and other ring structure.

The Voyager 1 radio occultation experiment obtained an analogous optical depth profile at microwave frequencies, by measuring the attenuation of dual-wavelength (3.6 and 13 cm) monochromatic radiation as the rings occulted the spacecraft (Tyler *et al.*, 1981, 1983). Once corrected for diffraction effects, the resolution achieved inward from the Encke Gap is ~400 m (Marouf *et al.*, 1986). Here a similar optical depth fluctuation pattern is found, although its wavelength and amplitude variations are less pronounced. In this data set the pattern is only detectible between 100 and 200 km inward from the inner gap edge, and the wavelength (2–4 km) is generally much shorter than in the observed PPS pattern.

We show in this paper that both of these observed patterns, as well as a third observed exterior to the Encke Gap in the PPS scan, are in good quantitative agreement with the behavior of a satellite wake as depicted in Fig. 1.2. By fitting these well-resolved patterns to a theoretical wake model, we obtain the orbit of the satellite responsible for each wake to high precision, as well an estimate of its mass. The fact that the orbit and mass determinations are in agreement with one another, as well as with those of CS based on the wavy edges, establishes the existence of an embedded moonlet within the Encke Gap beyond a reasonable doubt. The long time baseline between the Voyager 1 and 2 experiments makes it possible to specify the satellite's orbital period to extremely high accuracy. We point out that the methods used in this paper may be of use in inferring the presence of shepherding satellites near the Uranian rings from stellar or radio occultations, even if they are too small or dark to be detected directly by imaging.

In Section 2, we derive the theoretical model used to interpret the observations, while Appendix A contains estimates of self-gravity and collisional effects. A detailed, nonlinear wake theory, which treats self-gravity and collisions in a self-consistent manner, is beyond the scope of this paper. In Sections 3 and 4, we infer the moonlet's orbit and mass, respectively, based on our theoretical model and the observed data. In Section 5, we compare and summarize all of the data pertaining to the Encke Gap's (as yet) unseen moonlet.

2. PHYSICAL MODEL

2.1. Mass Density Distribution

When a ring particle on a circular orbit encounters a small, nearby satellite, the satellite's gravitational tug gives it an eccentricity e (Fig. 1.1). Afterward, its motion is described by epicycles about the guiding center of its motion. In a polar coordinate frame rotating with the satellite, the trajectory is described by

$$r(t) = a(1 - je \sin(\kappa t + \psi) + O(e^2)), \tag{2.1.1a}$$

$$\theta(t) = (\omega - \omega_s)t - 2je(\cos(\kappa t + \psi) - 1) + O(e^2), \tag{2.1.1b}$$

where the satellite is fixed at $\theta = 0$. Here $\omega_s \equiv \omega(a_s)$ is the orbital frequency of the satellite, which we also choose as that of the rotating reference frame. The epicyclic frequency $\kappa(a)$ differs from $\omega(a)$ due to Saturn's nonvanishing higher gravitational moments (J_2, J_4, etc.). Phase constant ψ will be discussed below. The parameter $j = \pm 1$ describes the radial direction from the satellite to the ring particle, meaning that $j = +1$ if $a > a_s$ and $j = -1$ otherwise. The above equations describe a particle's motion subsequent to the moonlet's impulse at $t = 0$; prior to the encounter, we assume that its eccentricity is zero. In reality, the satellite deflects a ring particle throughout roughly one orbital period surrounding $t = 0$; hence, the equations above do not apply in this interval. However, they are appropriate to describe the subsequent behavior, because the duration of the impulse is quite brief compared to the synodic period between successive satellite encounters.

We are concerned with the situation in which the induced radial motion ae of a ring particle is much smaller than the radial distance $|s|$ separating the ring particle and satellite, and this is in turn much smaller than the orbital radii a and a_s (see Fig. 1.1). It is useful to define the dimensionless parameter $\delta \equiv s/a_s = (a - a_s)/a_s$, which describes the separation of the ring and satellite orbits in terms of the overall scale of the system. Thus, we are interested in the situation where $e \ll |\delta| \ll 1$; this hierarchy of relationships determines the valid approximations to be used in the derivation below. For example, the 2-km radial wave amplitude observed at the Encke Gap edge (CS) corresponds to $e \sim 10^{-5}$; if the satellite falls near the center of the gap as they infer, then $\delta \sim 10^{-3}$.

If the perturbations of the moonlet are symmetric about $t = 0$, it can be shown that ψ vanishes in (2.1.1). [See also the numerical calculations of Showalter and Burns (1982).] In reality, the ring particle departs from the encounter with a nonzero eccentricity, which it did not have during its approach. This yields an asymmetry in the moonlet's attraction of $O(e/\delta)$, and it follows that ψ may also be of this (negligible) order.

Because the mass density fluctuations which arise from the satellite perturbations remain fixed in the rotating reference frame, it is appropriate to eliminate the time dependence from the trajectory equations, and write r as a function of θ instead. This is accomplished by first solving $\theta(t)$ (2.1.1b) for $t(\theta)$, and then substituting it into $r(t)$ (2.1.1a):

$$r = a\left(1 - je \sin \eta\theta + O\left(\frac{e^2}{\delta}\right)\right). \quad (2.1.2)$$

Here we have defined $\eta \equiv \kappa/(\omega - \omega_s)$, which is of order $1/\delta$. Note that $\eta\theta = \kappa t(1 + O(e))$.

The two quantities e and η are determined from the mechanics and geometry of the interaction. The induced eccentricity is approximated by

$$e \approx \frac{e_0\mu}{\delta^2} \quad (2.1.3)$$

[cf. Eq. (1.3 ff)], where μ is the ratio of satellite mass M_s to planetary mass M_p, and e_0 is the numerical coefficient 2.24. Note that $\mu \sim e\delta^2$, which is an extremely small quantity. Relative errors in (2.1.3) are of order δ and $J_2(r_p/a)^2$, where r_p is the planet's equatorial radius.

The azimuthal wavenumber η may be expanded as a power series in δ:

$$\eta(\delta) = \frac{\eta_0}{\delta} + \eta_1 + \eta_2\delta + \ldots . \quad (2.1.4)$$

Here the coefficients η_i depend upon the gravitational field of Saturn, and are all of order unity. Since $\eta\theta$ appears as the argument of a sine function, it must be evaluated to order unity, which requires the first two terms of the series. The coefficients may be evaluated from expansions of $\omega(a)$ and $\kappa(a)$ in Saturn's gravitational moments (cf. Lissauer and Cuzzi, 1982) and in powers of δ:

$$\eta_0 = -\frac{2}{3} + \frac{5}{3}J_2\left(\frac{r_p}{a_s}\right)^2 + \ldots \quad (2.1.5a)$$

$$\eta_1 = \frac{1}{6} + \ldots . \quad (2.1.5b)$$

Note that the J_2 term is required in the leading coefficient because, for our purposes, J_2/δ is not a small quantity.

When both the perturbing satellite and the ring particle begin on circular orbits, it can be shown that the ring particle's semimajor axis changes by $O(e^2/\delta) \approx 10^{-7}$, which is completely negligible for our purposes. Hence, we will assume that any ring particle streamline, designated by its semimajor axis a, maintains its identity during encounter. By continuity, the ring mass confined between two nearby streamlines which crosses any given longitude during brief time interval dt must be a constant, independent of the longitude (see Fig. 2.1). Before encounter, this mass is described by

$$dm_0 = \sigma_0(a) \cdot a\dot{\theta}_0 dt \cdot da, \quad (2.1.6a)$$

where the particles are bounded by radii a and $a + da$ and travel at azimuthal velocity $\dot{\theta}_0$. Afterward, it is described by

$$dm_1 = \sigma(a,\theta) \cdot r\dot{\theta} dt \cdot dr. \quad (2.1.6b)$$

Equating (2.1.6a) and (2.1.6b) and solving for σ yields

$$\sigma(a,\theta) = \sigma_0(a)\,\frac{a}{r}\,\frac{\dot{\theta}_0}{\dot{\theta}}\,\left.\frac{da}{dr}\right|_\theta. \quad (2.1.7)$$

We need to examine each factor in this expression individually. Mass density $\sigma_0(a)$ is the distribution before satellite encounter, which we have assumed to be azimuthally symmetric. (This requires that a moonlet's wake structure damp out in less than one synodic period). We also assume that any variation of σ and a is negligible on the radial wavelength scale of the structure induced by the satellite. By (2.1.2), the factor a/r is of the form $1 + O(e)$, which differs from unity by a negligible amount. The factor $\dot{\theta}_0/\dot{\theta}$ may be evaluated by differentiating (2.1.1b), and using $e = 0$ for the pre-encounter angular velocity $\dot{\theta}_0$. The result is an expression of the form $1 + O(e/\delta)$, which may also be neglected.

The final factor, $da/dr|_\theta$, is the only one which differs significantly from unity. Its reciprocal, which we will call h, is the derivative of (2.1.2):

$$h(a,\theta) \equiv \left.\frac{dr}{da}\right|_\theta = 1 + \left\{-jae\,\frac{d\eta}{da}\,\theta\right\}\cos\eta\theta + O\left(\delta, \frac{e}{\delta}\right). \quad (2.1.8)$$

We will identify the dimensionless coefficient in braces by Σ. Note that $d\eta/da \sim 1/a\delta^2$ [see (2.1.4) and (2.1.5)], so Σ is of order e/δ^2, not necessarily small compared to unity; indeed, $e \sim \delta^2$ is the requirement for significant variations in σ to arise.

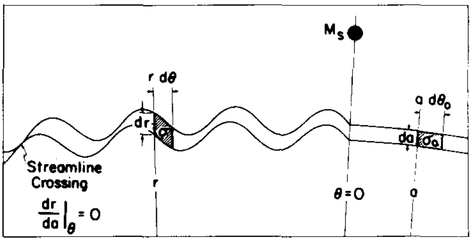

FIG. 2.1. The geometry of the local mass variation due to streamline compression and rarefaction. The two streamlines bound a strip of ring material within a moonlet wake. The shaded regions describe the same parcel of material before and after its encounter with the moonlet. Since the area it occupies changes while the mass is conserved, the surface density must vary accordingly. At a point where streamlines cross, the area becomes infinitesimal and the mass density would therefore become infinite. (Of course, one expects that collisions will prevent this from occurring.)

The quantity Σ is always positive, because $d\eta/da > 0$, and j and θ are of opposite signs in a wake which leads the satellite on the inside and trails it on the outside. It is also proportional to θ, which means that it increases monotonically as a ring particle drifts downstream from the moonlet. Streamlines will begin to collide when $h = 0$, where a nonzero range of a values falls atop a single radius (see Fig. 2.1). We define the critical longitude θ_{crit} as that value of θ at which h may first go to zero ($\Sigma = 1$). This locates the first point along a streamline where overlapping may occur:

$$\theta_{\text{crit}}(a) \equiv \left(-jae\,\frac{d\eta}{da}\right)^{-1} \approx \frac{\delta^2}{je\eta_0}, \quad (2.1.9)$$

where we have used (2.1.4).

Finally, combining (2.1.7)–(2.1.9) yields an expression for the local surface density of material:

$$\sigma(a,\theta) = \frac{\sigma_0(a)}{h(a,\theta)} = \frac{\sigma_0(a)}{1 + \Sigma(a,\theta)\cos(\eta(a)\theta)}, \quad (2.1.10)$$

where $\Sigma(a,\theta) = \theta/\theta_{\text{crit}}(a)$. This expression actually gives σ as a function of the semimajor axis a, which differs from the true radius r by $O(ae)$. Hence, to be precise, one must first convert r to a by inversion of (2.1.2), and then evaluate σ.

According to (2.1.10), the dimensionless parameter Σ equals the relative variation in mass density,

$$\Sigma = \frac{\sigma_{\max} - \sigma_{\min}}{\sigma_{\max} + \sigma_{\min}} \approx \frac{je_0\mu\eta_0\theta}{\delta^4}. \quad (2.1.11)$$

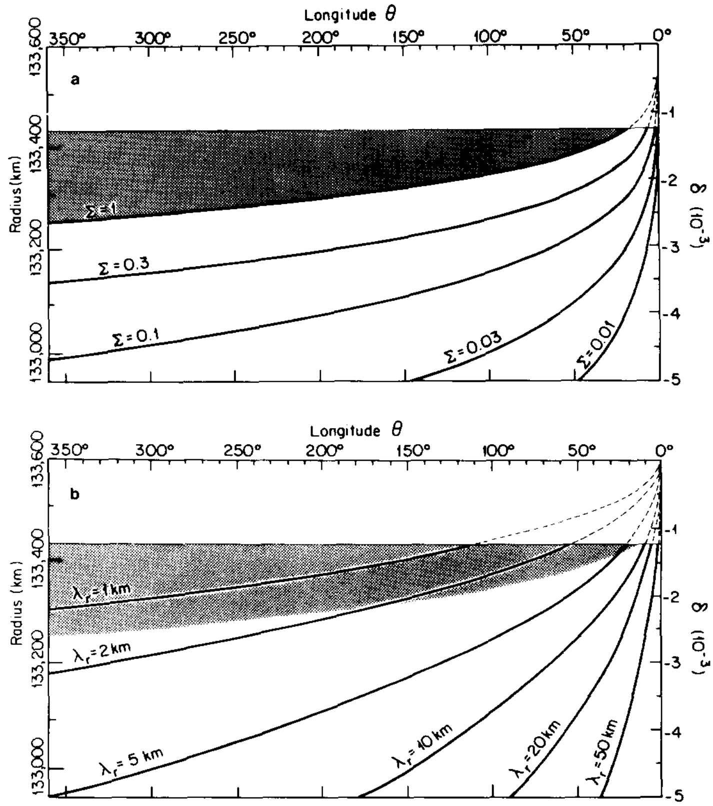

FIG. 2.2. The distribution of (a) density variation (Σ) and (b) radial wavelength (λ_r) in an interior moonlet wake, specified by contours of constant parameter value. The curves are based on Eqs. (2.1.11) and (2.2.7). Longitude from the satellite increases to the left and orbital radius increases upward in the diagrams; the moonlet itself occupies the upper right (and also upper left) corners. The shaded region is where streamline crossings are expected to occur, in this model which neglects all particle interactions. A moonlet mass of $5 \times 10^{-12} M_p$ is assumed for the calculations of Σ.

Note the very strong (δ^{-4}) dependence of Σ on the radial distance from the satellite. As δ increases, the eccentricity decreases as δ^{-2}, the number of wavelengths traversed by a particle at a given longitude decreases as δ^{-1}, and the fractional phase shift with radial distance also decreases as δ^{-1}. Equation (2.1.10) indicates that, near streamline crossing, $\sigma_{\min}$ approaches half of the background surface density σ_0, while $\sigma_{\max}$ approaches infinity. This is similar to the situation for strongly nonlinear density waves (Shu *et al.*, 1985). Figure 2.2a shows the distribution of Σ values within a typical satellite wake.

2.2. Density Extrema on a Linear Profile

The Voyager 1 radio occultation and the Voyager 2 PPS stellar occultation experiments both yield profiles of ring optical depth along narrow tracks across the ring system. These tracks are not radial, however, either in inertial space or in the frame of an orbiting satellite. Here we will use the quantitative model just derived to determine the locations of density extrema along such off-radial tracks.

We describe the direction of a scan by the angle α it makes with the radial direction, in a frame rotating with the moonlet. Since the moonlet's motion is not negligible over the time it takes to scan the region, this angle differs significantly from that determined in an inertial frame. Alternatively, we may describe the scan direction by a unit vector $\mathbf{s}$, with radial and tangential components ($\cos\alpha$, $\sin\alpha$). The extrema on the scan must occur where

$$\mathbf{s}\cdot\nabla\sigma = 0. \qquad (2.2.1)$$

Recall from (2.1.10) that $\sigma = \sigma_0(a)/h(a,\theta)$, where $\sigma_0(a)$ varies negligibly on the distance scale of a single wavelength. Hence (2.2.1) is equivalent to $\mathbf{s}\cdot\nabla h = 0$, which is considerably easier to evaluate. Expanding the dot product yields

$$\frac{\partial h}{\partial r}\cos\alpha + \frac{1}{r}\frac{\partial h}{\partial\theta}\sin\alpha = 0. \qquad (2.2.2)$$

In evaluating the derivatives of h, it is convenient to define $u \equiv 1/\delta = a_s/(a - a_s)$, which is intrinsically a large quantity. In terms of this variable,

$$h = 1 - je_0\mu\eta_0\theta u^4\cos([\eta_0 u + \eta_1]\theta) \qquad (2.2.3)$$

[by (2.1.3), (2.1.4), and (2.1.8)]. When taking the partial derivatives for (2.2.2), it is important to recall the distinction between radial coordinate r and semimajor axis a. The radial derivative becomes

$$\frac{\partial h}{\partial r} = \frac{1}{h}\frac{dh}{da}\bigg|_\theta = \frac{je_0\mu\eta_0\theta}{ha_s}u^6\eta_0\theta\sin\eta\theta, \qquad (2.2.4)$$

where we have neglected a term of lower order in u. The highest order term in the azimuthal component of (2.2.2) is found to be proportional to u^5, which may be neglected compared to the radial component above as long as $\cos\alpha \gg \delta\sin\alpha$ (i.e., the scan direction is not extremely close to azimuthal, $\alpha \approx 90°$). This is not surprising, since a moonlet wake is very nearly axisymmetric. Thus, the extrema on a scan generally occur where $\partial h/\partial r = 0$. By (2.2.4), this is equivalent to $\sin\eta\theta = 0$, or simply

$$\eta(a)\theta = m\pi, \qquad (2.2.5)$$

for nonnegative integer m. By (2.1.10), it is clear that density minima occur where the "extremum index" m is even and maxima occur where it is odd (see Fig. 1.2). Note also that $r = a$ whenever $\sin\eta\theta = 0$ (by 2.1.2), so that solving (2.2.5) above for a yields r directly; it appears that a ring particle passes through an extremum whenever it returns to its semimajor axis, as is seen in Fig. 1.2. Also, since the extremum locations do not depend on the amplitude ae of the radial oscillations, they have the useful property of being independent of the perturbing satellite's mass.

To solve (2.2.5), we replace η by the first two terms of its power expansion (2.1.4). This yields

$$u_m = \frac{m\pi}{\eta_0\theta} - \frac{\eta_1}{\eta_0} + O(\delta), \qquad (2.2.6)$$

where $r_m = a_m = a_s(1 + 1/u_m)$. Based on this result, the rough wavelength variation on a linear scan is found to be

$$\lambda_r = |r_{m+1} - r_{m-1}| \approx 3\pi a_s\frac{\delta^2}{|\theta|}\left(1 - \left|\frac{\delta}{\theta}\right|\tan\alpha\right). \qquad (2.2.7)$$

Note that the wavelength increases quadratically with the radial distance to the satellite, and decreases inversely with the azimuthal distance. The wavelength depends only weakly on the scan direction, provided that α does not approach the pitch angle of the crests and troughs. In general, λ_r decreases for $\alpha > 0$ and increases for $\alpha < 0$. The wavelength variation within a typical wake pattern is shown in Fig. 2.2b.

2.3. *Limitations of the Model*

We now critically examine some of the assumptions which went into the model derivation.

In using the simple expression (2.1.3) for the eccentricity induced by the satellite, we have ignored the possibility that this body may have a nonvanishing eccentricity of its own. If its eccentricity is e_s, then (2.1.3) will have relative errors of order e_s/δ (cf. Showalter and Burns, 1982; Showalter, 1984). But more importantly, nonzero e_s invalidates the assumption that the semimajor axis of each ring particle is unchanged after passage of the satellite. Since streamlines do not maintain their identity past the moonlet, most of the derivation of $\sigma(r, \theta)$ in Section 2.1 is no longer appropriate. This is analogous to the effects observed in Showalter and Burns' numerical simulation of the F Ring; eccentricity in the nearby shepherding satellites induces a clumping of the F Ring material which does not occur when they follow circular orbits. Exactly what nonzero eccentricity would do to the satellite wake pattern is as yet unclear, but the effect could be quite pronounced. This problem will not be important provided the radial excursions of the satellite $a_s e_s$ are an insignificant fraction of the distance to the edge of the gap. Turning the problem around, the fact that we observe the patterns in the PPS and radio data suggests that e_s is small. Perhaps this is not surprising; theoretical expectations are that the net transfer of angular momentum between the moonlet and adjacent ring material at a combination of Lindblad and corotation resonances would preferentially damp the moonlet's eccentricity to zero (Goldreich and Tremaine, 1980).

A more important issue is the relative importance of collective effects among the ring particles, such as self-gravity and collisions; our analysis assumes that streamlines do not interact. Although collective effects are not required for the wake pattern to arise or persist, they may play a significant role in its detailed evolution. Naively, collisional damping would be expected to increase rapidly after the point at which streamlines begin to cross. However, the Encke Gap's observed wavy edges survive for roughly 270° of azimuth, although with diminishing amplitude (CS). This is much greater than the 10–20 wavelengths expected before streamline crossings should occur. The likely reason why the radial oscillations persist is that the collisions do not commence suddenly at the critical longitude predicted for noninteracting streamlines. In reality, collisions between particles increase gradually as neighboring streamlines approach; however, the colliding particles are traveling at nearly the same velocities, so collisions are very gentle and not disruptive to the wake pattern. Instead, they probably tend to modify the phase relationship between neighboring streamlines, and thereby prevent or delay the more violent and disruptive collisions from occurring. In a similar way, it is possible that the self-gravity of the ring material may have an effect on the morphology of the wavy edges. The existence of spiral density and bending waves near the Encke gap implies that local enhancements of density, of the proper morphology, may be self-enhancing.

Due to these collisional and self-gravity effects, it is reasonable to expect the observed wake structure to deviate somewhat from the quantitative model just derived, particularly in regions where Σ is close to unity. Appendix A contains a more rigorous assessment of these effects. In summary, we regard our derived model as a good approximation to the actual situation, particularly when not far from the moonlet; observed discrepancies between the model and observations may provide clues as to the nature of a more complete, self-consistent solution.

3. MOONLET ORBIT DETERMINATION

3.1. Data Analysis Procedure

The quantitative model just described allows one to predict the resultant mass density distribution in a ring, neglecting collective effects, given the orbit and mass of a perturbing moonlet. We are confronted with the inverse problem, which is to solve for a moonlet's properties, given profiles of the wake pattern it produced.

Both the PPS and radio scans may be construed as measurements of normal opti-

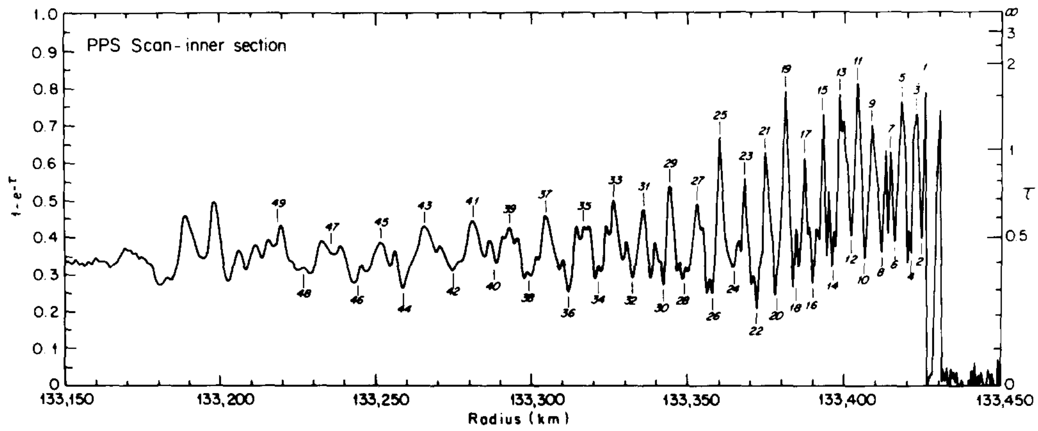

FIG. 3.1. A radial profile of ring optical depth τ just interior to the Encke Gap, as determined from the Voyager 2 stellar occultation (PPS) scan. A moonlet wake is visible starting at the gap edge, and shows the characteristic increasing wavelength and decreasing amplitude with distance from the gap. A narrow detached ringlet just outside the gap edge appears to be unrelated to this pattern. Extrema are numbered 1 through 49. This plot was generated by smoothing the data with a variable-width filter, specifically chosen to mimic the changing wavelength; the entire wake cannot be shown to its best advantage using a single filter width.

cal depth τ as a function of position in the ring. Since τ is proportional to mass density σ (assuming an invariant size distribution), our model for $\sigma(r, \theta)$ (2.1.10) is readily converted to one for $\tau(r, \theta)$. In principle, it is possible to fit each scan directly to the model, yielding four unknowns: a_s, M_s, satellite longitude ϕ_s at a given epoch, and also τ_0, the ring's unperturbed optical depth. However, this is not a desirable approach for several reasons. First, τ_0 may actually be an arbitrary function of radius; although we assume that it varies slowly over the scale of a single wavelength, we have no reason to assume that it is constant throughout the regions of interest. But more importantly, we expect collective effects, such as viscosity and self-gravity, to become important (at least) near streamline crossing (see Appendix A).

For these reasons as well as computational efficiency, we break the task down into two separate parameter fits. First, we determine the satellite's orbit based exclusively upon the measured locations of extrema in the scans. As shown in Section 2.2, these locations depend on a_s and ϕ_s, but not on M_s or τ_0. Second, given the orbit, we perform direct fits to subsets of the scans to specify τ_0 and M_s; for small enough subsets of the data, any variation in τ_0 should be negligible. In addition, this two-step approach allows us to better recognize where and how the model breaks down due to collective effects.

3.2. The Inner PPS Scan

The most notable profile of a wakelike pattern is found in the Voyager 2 PPS scan, just interior to the Encke Gap. It was first recognized very shortly after the Saturn encounter, and was described by Lane *et al.* (1982, see their Fig. 9), although no explanation for the feature existed at the time.

The PPS scan is a list of numbers of photons counted by Voyager 2's photopolarimeter, as it observed the star δ Scorpii through Saturn's rings (Lane *et al.*, 1982). Due to the motion of the spacecraft, each 10-msec count interval sampled a radial distance of ~100 m in the ring. The structure we analyze extends over a distance of 200 km and therefore covers 2000 PPS samples; it is shown in Fig. 3.1. Since

TABLE I

ENCKE GAP SCAN GEOMETRY

Parameter		PPS scan	Radio scan	Units
Reference radius[a]	r_{ref}	133,459.3	133,487.2	km
Reference longitude[a,b]	ϕ_{ref}	171.827	222.496	deg
Reference time[a,c]	t_{ref}	1981/238	1980/318	y/d
		1:38:23.4	3:33:02.3	h:m:s
Scan radial velocity	$\dot{r}$	9.426	82.38	km/sec
Scan direction	$\alpha_{\mathrm{inertial}}$	11.8	−27.6	deg
	$\alpha_{\mathrm{moonlet}}$	−57.6	−36.0	deg
Effective resolution		94.26	400	m
"Bin" size		94.26	200	m
Gap inner edge		133,425.8	133,433	km
Gap outer edge		133,752.5	133,755	km
Gap width		326.7	322	km

[a] Reference values apply to an arbitrarily chosen point within the Encke Gap along each occultation track.

[b] In the EME50 frame.

[c] Spacecraft event time (UT).

the wavelength ranges from 5 to 20 km within the scan, it is well-resolved by the 100-m data bins. Table I lists various attributes of this scan's geometry, determined by J. Holberg (private communication, 1985) using Saturn's recently revised pole position (Simpson *et al.*, 1983). Longitudes are given in the coordinate frame defined by the Earth's mean equator and equinox of 1950 (EME50; see Appendix B).

We have labeled each of the extrema in this scan sequentially by a feature index i, as is shown in Fig. 3.1. These indices increase with distance from the gap, with even numbers identifying optical depth minima and odd numbers identifying maxima. Aside from these properties, the specific value of i associated with a given feature is arbitrary. We measure the precise radial location R_i of each extremum by convolving the raw data with a range of broad filters to diminish the noise; from feature to feature, the optimal filter width varies in proportion to the local wavelength.

Before performing the fit, it is important to know the approximate uncertainty in each measurement. Although we may know the uncertainty in each optical depth value from the noise properties of the data, it is very difficult to infer the error in the radial location of a peak after severe filtering; instead, we estimate mean errors empirically from the measurements. Each R_i may be regarded as a random variable, having a standard deviation σ_i which varies only slightly from one point to the next. Noting that each extremum should fall roughly halfway between its nearest neighbors, we define another random variable X_i as

$$X_i \equiv \frac{1}{2}(R_{i+1} + R_{i-1}) - R_i. \quad (3.2.1)$$

If the variation in wavelength over the distance scale of a single wavelength is small, then X_i has an expectation value $E(X_i) \ll \lambda_r$, and a variance

$$\mathrm{var}(X_i) \approx \frac{3}{2}\sigma_i^2. \quad (3.2.2)$$

Hence, studying the scatter in X_i should allow us to estimate the measurement uncertainties σ_i. Note that, since $E(X_i)$ does not precisely vanish, this procedure may yield a slight overestimate of the variance.

In the PPS data, we note that the scatter in X_i increases in proportion to the local radial wavelength λ_r (approximated by $[R_{i-1} - R_{i+1}]$). This is not surprising, because at longer wavelengths the wave amplitude is smaller, making individual extrema harder to pinpoint. Thus, extremum measurements closer to the gap edge are relatively more accurate, and should be weighted accordingly. We find empirically that the standard deviation $\sigma_i \approx 0.04\lambda_r$ in the PPS scan, meaning that measurements are typically accurate to 4% of the local wavelength.

A straightforward weighted nonlinear least-squares fit to the measurements R_i may now be performed. Three unknown parameters are sought: a_s, ϕ_s at the measurement epoch, and a reference index m_{ref}. This reference index is chosen to relate the extremum index m_i to each feature i: $m_i = m_{\mathrm{ref}} - i$. We know a priori that m_{ref} must be an even integer, since optical depth minima (even m_i) are designated by even i.

TABLE II

SATELLITE ORBIT PARAMETERS[a]

Feature range i	Extremum reference m_{ref}	Orbital radius a_s (km)	Longitude[b] ϕ_s (°)	GOF
		PPS scan—inner section		
2–49	90.42 ± 0.32	133,605.4 ± 1.2	139.26 ± 0.33	1.16
14–49	89.87 ± 0.39	133,602.2 ± 1.9	139.95 ± 0.44	0.86
14–49	88	133,593.5 ± 0.4	142.02 ± 0.05	1.12
14–49	90	133,602.8 ± 0.3	139.81 ± 0.04	0.85
14–49	92	133,612.1 ± 0.4	137.53 ± 0.06	1.15
		PPS scan—outer section		
1–140[c]	447.6 ± 1.4	133,580.2 ± 1.8	155.2 ± 2.8	1.58
29–140[c]	447.9 ± 2.0	133,579.9 ± 2.5	155.6 ± 3.8	1.28
		Radio scan		
2–88	288.5 ± 2.2	133,597.7 ± 3.0	66.7 ± 2.9	1.34
2–86[d]	287.9 ± 2.4	133,597.0 ± 3.2	67.4 ± 3.2	1.00

[a] All uncertainties quoted are formal 1-σ values. They are rescaled by the goodness of fit to account for possible inadequacy of the model and uncertainty of the inferred measurement errors.

[b] In the EME50 frame, at the reference time listed in Table 1 for each scan.

[c] Features 111–114 are not visible in the scan, and are omitted from the fit.

[d] Parameter fit using only density minima (i.e., even i).

Nevertheless, we allow it to float freely in the parameter fits. Note also that, in the fitting procedure, the actual longitudinal distance $\theta \equiv \phi - \phi_s$ between scan and moonlet must be recalculated at each point on the scan; the moonlet is moving and the scans are nonradial, so both ϕ and ϕ_s change slightly from one point to the next.

Table II lists the parameter values resulting from the fit on features 2 through 49 of the PPS scan, along with their inferred uncertainties. Feature 1, the first density maximum inward from the gap, has been found to correspond to the location where the gap edge truncates the wake structure; since it is not a moonlet-derived maximum, it is omitted from this and subsequent solutions. The overall goodness of fit (GOF) is 1.15; this is defined as the square root of χ^2/N, where χ^2 is the sum of squared fit residuals in units of the standard deviation, and $N = 48 - 3$ is the number of degrees of freedom in the fit. Thus, GOF is equivalent to the RMS fit residual. This value suggests that either the error has been underestimated by 15%, or the model does not accurately describe the data. The former explanation is unlikely for reasons cited above. To check the latter possibility, we plot the residual for each measurement in Fig. 3.2. Note the large jump in residuals near $i = 13$. A reexamination of the PPS scan shows that the measurements are accurate, but that the character of the wake seems to change near this location. Note the small phase shift and the change in mean optical depth visible between features 13 and 14 in the scan (Fig. 3.1). We regard this as evidence that streamline interactions are beginning to become important, and that our model is no longer appropriate in the outer portion of this scan ($i \leq 13$).

We next perform the fit only on features 14 through 49; the results are again shown in Table II. Now the GOF drops to 0.86, implying that our error bars were slightly overestimated (as expected). The best fit value for m_{ref} is 89.9 ± 0.4, which appears quite consistent with 90, but inconsistent with the nearest other possibilities, 88 and 92. Finally, we lock m_{ref} on each of these three discrete values, and determine the best fit for the remaining two unknowns. Results are listed in the table. The GOF changes negligibly for $m_{\text{ref}} \equiv 90$, but is unreasonably large for the other two values. Figure 3.3 is a plot of the residuals for each m_{ref} value, much like Fig. 3.2. For $m_{\text{ref}} \equiv 88$

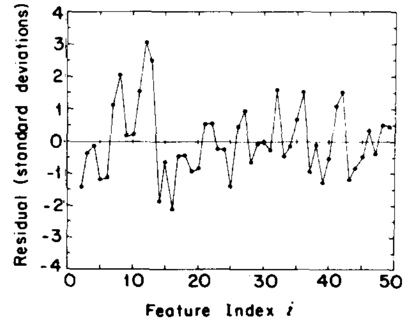

FIG. 3.2. A plot of the measurement residuals from the initial orbit fit to features 2–49. Note the large jump between features 13 and 14, which corresponds to a phase shift in the wake.

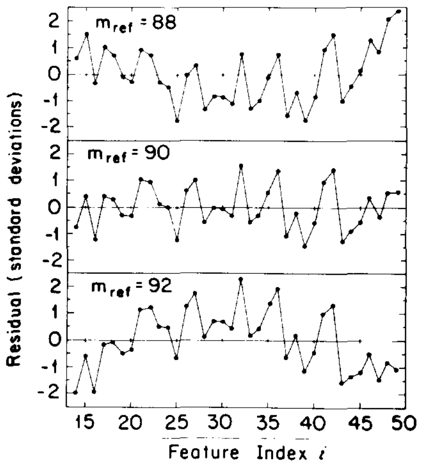

FIG. 3.3. Plots of the best fit residuals, when the parameter m_{ref} is held fixed at each of three plausible values. The general upward curvature for $m_{\mathrm{ref}} = 88$ and the downward curvature for $m_{\mathrm{ref}} = 92$ imply correlated residuals, and hence an inadequate fit to the data.

or 92, the significant correlation between neighboring residuals provides strong indication that the model is not correct; these parameter values do not allow for a statistically plausible fit to the data, and may therefore be rejected.

Apparently, the first minimum (feature 2) lies exactly 44 azimuthal wavelengths downstream from the moonlet. Overall, the moonlet falls 14 km outside the center of the Encke Gap, and 32° away from the scan. (See Appendix A for a discussion of the error in moonlet longitude due to collective effects.)

3.3. The Outer PPS Scan

We have shown that the wakelike pattern observed just inward from the Encke Gap in the PPS scan can be explained by the influence of a satellite which trails the scan by 32°. Recall that a moonlet's wake should lead it on a gap's inner edge and trail it on the outer edge. Thus, one might expect to see the wake of the same moonlet, 328° away in the opposite direction, outside the Encke Gap. Such a wake is expected to have a wavelength of ~2 km (see Fig. 2.2), although streamline interactions would probably destroy the pattern in the section closest to the gap edge, as they have apparently destroyed most of the edge ripples at this longitude (CS).

Figure 3.4 shows a portion of the PPS scan outside the gap. A region of quasiperiodic optical depth variations is indeed visible, with a radial wavelength of 2–3 km, commencing roughly 200 km outside the gap edge. Large variations in optical depth are evident beyond both ends of this region, but they do not display the near-periodicity characteristic of a moonlet wake.

We analyze this structure in the manner described in Section 3.2. Feature index values (ranging from 1 to 140) are shown in the figure, although several intermediate extrema (111–114) seem to be missing; apparently noise or other physical processes determine the ring's structure in this limited radial range. This wake is still well resolved by the 100-m PPS data bins; however, due to the shorter wavelength, the inferred uncertainty in extremum locations is $\sim 0.06\lambda_r$, somewhat larger than for the interior PPS wake.

An initial fit to feature locations 1–110 and 115–140 leads to the moonlet orbit listed in Table II. The large GOF (1.58) indicates that some aspect of the model is inconsistent with the data. As before, a plot of the residuals reveals an abrupt phase shift in the outer section of the wavetrain, near $i = 27$, as can be seen in Fig. 3.4. The results of a new fit, after eliminating all features below the 29th, are shown in the table. The GOF improves considerably (to 1.28), but residuals are still too large. There appears to be a real, systematic deviation between our simple model and this moonlet wake structure. At this great a distance from the moonlet, and with such rapid radial fluctuations, such a deviation should not be too surprising.

The best fit parameter values indicate that the moonlet is 344° ± 4° away from the scan, in contradiction to our belief that it is

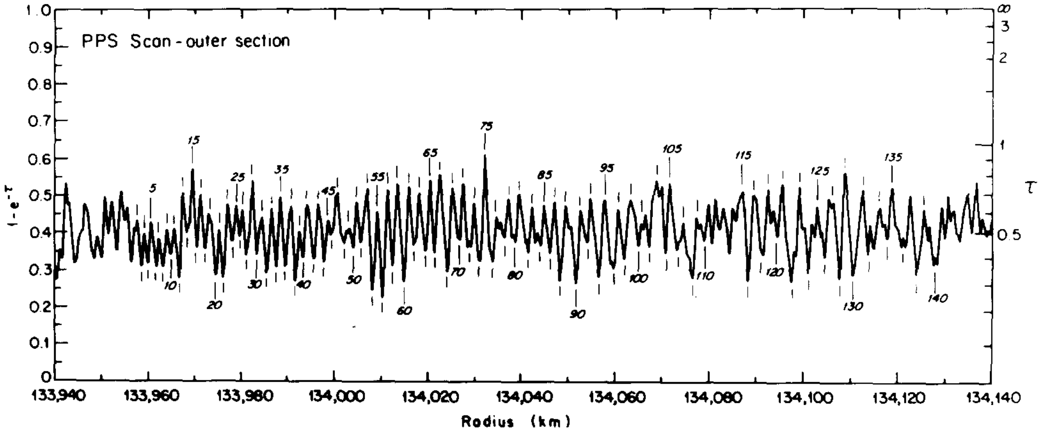

FIG. 3.4. A radial profile of ring optical depth, beginning roughly 200 km outside the Encke Gap, as determined from the PPS scan. To diminish noise, the scan has been convolved with a 1-km-wide filter. Extrema are numbered 1 through 140, except for features 111–114 which cannot be identified. Large variations in optical depth persist on both sides of the numbered region, but the expected near periodicity of a moonlet wake is not visible. Apparently, collective effects have destroyed the wake inward from the numbered region, while other physical processes dominate beyond the wake's outer limit.

actually 328° away. Note that the semimajor axis determinations also differ, by 23 km. Nevertheless, it is absurd to conclude that these are distinct bodies; two moonlets this close together (and of comparable mass, as will be shown in Section 4) would generate interfering wake patterns on both sides of the gap, and the scans would look very different.

We expect any orbit determination based on a scan so far from the moonlet to be unreliable, since collective effects would have had ample opportunity to modify the arrangement of streamlines within the wake. The large residuals seem to confirm that some modification has taken place. Nevertheless, the deviation from our naive model after 328° of longitude is surprisingly small. The wavelengths observed in this scan range from 4 to 8% longer than would be expected from the previously derived orbit. That ratio decreases monotonically with increasing radial distance from the moonlet, which is to be expected, since collective modifications will be reduced (and our model more accurate) where the wake amplitude is smaller.

The presence of a wake so far downstream from the moonlet has an important logical consequence; it indicates that only a single dominant body orbits within the gap. Any other large body would have had to be nearer in azimuth, and therefore would have generated a more prominent wake outside the Encke Gap.

3.4. *The Radio Scan*

The Voyager 1 radio occultation, though similar to the PPS scan in principle, is a very different sort of experiment. Because of the coherency of the radio signals generated onboard Voyager, both the amplitude and the phase of the signal component that directly propagates through the rings may be identified and separated from the Doppler-broadened component scattered by ring particles just off the line of sight (Tyler *et al.*, 1981; Marouf *et al.*, 1982). The measured time history of signal amplitude and phase actually corresponds to a sampled one-dimensional microwave hologram formed behind the rings. Proper reconstruction of this hologram results in a microwave optical depth profile whose radial

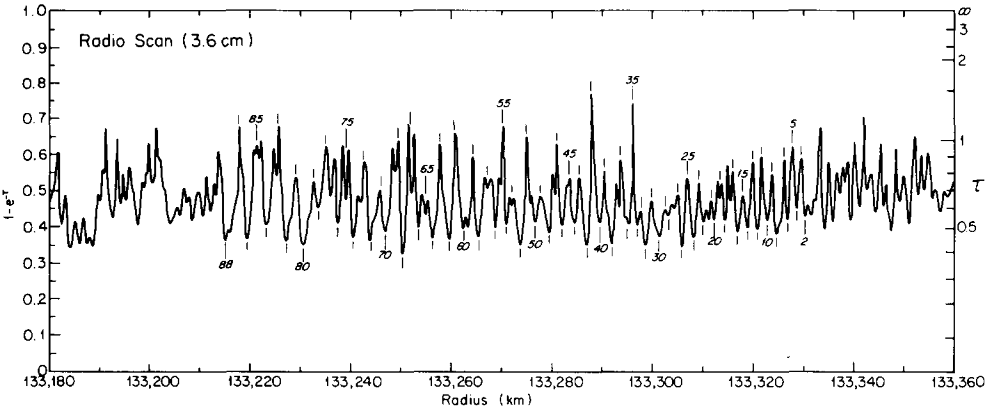

FIG. 3.5. A 3.6-cm-wavelength optical depth profile of the ring from the Voyager 1 radio occultation experiment, ending ~80 km inward from the Encke Gap. For display, the scan has been smoothed with a 1-km filter. Extrema numbered 2 through 88 appear to be part of a wake pattern. As in the outer PPS scan (Fig. 3.4), unrelated structure is visible beyond both ends of the numbered region.

resolution varies from 200 m to a few kilometers, depending on the transparency of the region occulted (Marouf *et al.*, 1985).

The 3.6-cm-wavelength data set which we examine spans 250 km of radius just inside the Encke Gap inner edge, and is sampled every 200 m; however, the effective radial resolution achieved in the reconstruction process in actually ~400 m (Marouf *et al.*, 1986). Figure 3.5 shows the relevant 180-km section of the data, with extrema numbered 2 through 88; Table I lists relevant geometric parameters of the scan. As in the case of the outer PPS scan, this wake is apparently destroyed by collective effects at its outer limit, and is obscured by unrelated ring structure at its inner limit. Here the wavelength measured ranges from 2 to 4 km. Examination of scatter in the X parameter (3.2.1) shows the error to be nearly independent of wavelength, and with an amplitude $\sigma_i \approx 200$ m, the size of a single data bin. Apparently, it is the scan's intrinsic radial resolution which limits the measurement accuracy attainable. Hence, in the fit to this scan, each extremum measurement is weighted equally.

Table II lists the parameter values resulting from a fit to all of the extrema located in the radio scan. The GOF is a disappointing 1.34, but an examination of the fit residuals reveals a notable property: nearly all of the largest residuals occur at odd features, which correspond to optical depth maxima. Because Saturn's rings were only 5.9° open as seen from Earth at the time of the Voyager 1 radio occultation, optical depth along the line of sight is magnified by ~10 times it normal value. This results in opacity maxima (odd-numbered features) which are most highly affected by noise. One could simply repeat the fit giving odd-numbered features a smaller weight; however, considering the large number of extrema located, it is reasonable to simply omit all of these measurements. The only large residual on an even-numbered feature occurs at $i = 88$, which is the innermost point measured. It is quite plausible that this location is modified by whatever process terminates the wake; we therefore also eliminate it from subsequent fits.

Forty-three measurements remain for determining the satellite's orbit. The results of a new fit are listed in Table II. The GOF drops to 1.00, indicating that the model provides a satisfactory description of the data. Unfortunately, the large formal error on m_{ref} makes it impossible to specify the precise number of azimuthal wavelengths between the scan and the moonlet, as was possible for the inner PPS scan. This is a consequence of the lack of a strong radial wavelength variation within this scan, so that a shift of the model pattern by a small whole number of wavelengths does not severely degrade the GOF.

According to the model, this scan falls 155° downstream from the moonlet, which is somewhat intermediate between the inner and outer sections of the PPS scan. We would therefore expect collective effects to be intermediate in importance. Since collective effects increase the local wavelength by $\sim 5\%$ in the outer PPS scan, it would not be surprising if a comparable error is present here, and the derived orbit would be correspondingly incorrect. Unfortunately, the region outside the Encke Gap is too optically thick at the radio wavelength to detect the corresponding outer wake; hence we have no independent confirmation of a systematic error caused by collective effects, as we did for the two PPS scans. Nevertheless, we examine this possible offset below.

3.5. Comparison of Orbits

In this section, we compare the moonlet orbits determined above with one another, as well as with that inferred from the locations of the wavy edges (CS). From the inner and outer sections of the PPS scan alone, it is clear that only one dominant moonlet orbits within the gap; this confirms the inferences of Cuzzi and Scargle.

The most reliable determination of the orbit comes from the inner region of the PPS scan, because here the moonlet is only 32° away. In Appendix A, we show that collective effects are probably negligible at this small distance. The moonlet's semimajor axis a_s is found to be 133,603 ± 10 km. Although the parameter fit yielded a formal 1-σ uncertainty of less than 1 km, the above more reasonable error bar incorporates the systematic uncertainty in the radial scale of the PPS scan, which Simpson *et al.* (1983) estimate to be <10 km. The semimajor axis corresponds to a mean motion of 625.90 ± 0.07°/day, based on a Voyager-derived value for Saturn's mass ($GM_p = 3.79312 \times 10^7$ km^3 sec^{-2}; J. D. Anderson, private communication, 1985) and gravitational moments given by Lissauer and Cuzzi (1982; cf. Null *et al.*, 1981).

The simplest comparison to be made is between the moonlet longitudes derived from the PPS scan and the distribution of wavy edges, since the latter were observed primarily by Voyager 2. Cuzzi and Scargle (1985) give longitudes in the coordinate frame specified by solar hour angle (SHA) at the time of Voyager 2 periapsis (Spacecraft Event Time 1981/238/3:24:08.0), which occurs 6344.6 sec after the reference time for the PPS scan (see Table I). Extrapolation of the PPS-derived orbit to this time puts the satellite at EME50 longitude 186°. Cuzzi and Scargle infer that the dominant moonlet falls between SHA 343° and 16°, which is 190° ± 16° in the EME50 frame (see Appendix B). The match is clearly quite satisfactory.

A comparison of the PPS- and radio-derived orbits is more challenging, due to the long time baseline separating the Voyager 1 and 2 observations. The reference times for these experiments are separated by 24,703,521.1 sec, in which time the satellite traversed 497 orbits plus 38° ± 20°. This places the moonlet at EME50 longitude 102° ± 20° at the time of the radio scan, whereas the fit to the radio data places it at 67° ± 3°. The 35° discrepancy is small, but somewhat larger than the experimental uncertainty (which is based upon the firm error limit of Simpson *et al.*, 1983). Of course, it would not be surprising to find that our radio-derived orbit is somewhat erroneous due to neglected ring particle interactions. A 15° offset of the moonlet closer to the radio scan location would place it within the error bar, and is similar in magnitude and direction to the correction for collective effects in the outer PPS scan.

However, results are less favorable when one compares the observed wavelengths with those expected from the PPS-derived orbit. In the data, the wavelength ranges from 1.8 to 3.6 km with radius, whereas the most favorable theoretical estimates (established by positioning the moonlet at the end of its error bar) range from 2.1 to 4.2 km. Thus the predicted wavelength is at least 17% too large in the radio scan, while it is 4–8% too small in the more distant PPS scan. Although it is not impossible for the ill-understood collective effects to explain both of these observations, it is surprising that they should be greater in magnitude and opposite in sign nearer to the moonlet. Alternatively, the precise radial reference for both scans may be less accurate than has been previously supposed; a mean motion of 626.02°/day is needed to make the Voyager 1 and 2 longitudes coincide, which corresponds to a radius of 133,586 km.

Despite the quantitative discrepancy, the error of 35° in longitude is a tiny fraction of the 497 elapsed orbits. It remains exceedingly likely that a single moonlet is responsible for all three wakes detected near the Encke Gap, as well as all of the observed wavy edges.

4. MOONLET MASS DETERMINATION

4.1. Procedure

We have determined the satellite's orbit from the locations of extrema in the scans. We now wish to establish its mass, based primarily upon the amplitude of the observed variations in optical depth. This is simplest using the unsmoothed data, because the act of averaging together neighboring bins tends to reduce the overall amplitude of the waves. We therefore fit directly to individual PPS count values.

By (2.1.10), the ring's optical depth at any location may be modeled by

$$\tau(r,\theta) = \frac{\tau_0(a)}{1 + \mu g(a,\theta)}, \qquad (4.1.1)$$

where the satellite mass is found by $M_s = \mu M_p$. The function $g(a, \theta) = je_0\eta_0\theta \cos(\eta\theta)/\delta^4$ depends only on known geometrical parameters. It is necessary here to distinguish between a and r; note that the function $a(r, \theta)$, found by inverting (2.1.2), also depends weakly on the satellite mass.

The number of photons k counted in a single PPS data bin is related to the optical depth by

$$k = k_{\mathrm{ref}} e^{-\tau/\sin B} + k_{\mathrm{bg}}, \qquad (4.1.2)$$

where $k_{\mathrm{ref}} \approx 39$ is the mean number of photons from the unobscured star, $k_{\mathrm{bg}} \approx 6.65$ is the number of background counts expected even when the star is completely blocked, and $B \approx 29°$ is the angle between the ring plane and the line of sight. By substituting (4.1.1) into (4.1.2), we establish a theoretical model for k at a point in the ring as a function of two unknowns, τ_0 (assumed constant over a limited region) and μ.

Once again, the uncertainties in measurement values are more difficult to determine than the measurements themselves. Since each PPS bin counts a discrete (and small) number of photons, one might expect Poisson statistics to apply, in which case the variance $\sigma_k^2 = \bar{k}$, where $\bar{k}$ is the expected number of counts. This may be tested easily. Within the PPS scan, the local mean optical depth $\bar{\tau}$ [related to $\bar{k}$ via (4.1.2)] should vary rather little from one bin to the next; therefore, two neighboring PPS count values k_l and k_{l+1} may be regarded as independent, identically distributed random variables. It can be shown that the expectation

$$E[(k_l - k_{l+1})^2] = 2\sigma_k^2(\bar{k}). \qquad (4.1.3)$$

Thus, we can estimate σ_k as a function of $\bar{k}$ by

$$\hat{\sigma}_k^2(\hat{k}) \approx \frac{1}{2N} \sum (k_l - k_{l+1})^2, \qquad (4.1.4)$$

where, for a given $\hat{k}$, the sum is over the N pairs of neighboring PPS counts for which $(k_l + k_{l+1})/2 = \hat{k}$. It can be shown that the formal distinction between the sample mean $\hat{k}$ and the true (but unknown) mean $\bar{k}$

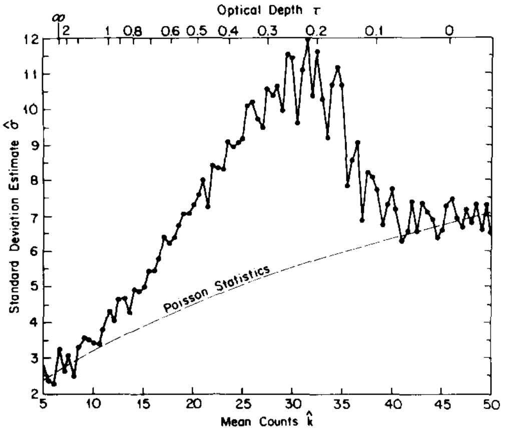

FIG. 4.1. The statistical scatter in PPS counts observed in the Encke Gap neighborhood, as described in Section 4.1. At intermediate optical depths, the scatter between neighboring PPS bins is clearly much larger than may be accounted for by Poisson statistics.

does not significantly bias such a tabulation. Figure 4.1 is a plot of the standard deviation estimate $\hat{\sigma}_k$ as a function of $\hat{k}$, based on PPS data throughout the Encke Gap region. A reference curve for Poisson statistics is also shown. The data and the curve match for τ near 0 or ∞, but are clearly incompatible at intermediate values; here the scatter between neighboring PPS bins is substantially greater than may be accounted for by photon counting statistics.

This curve could be explained by a preponderance of unresolved structure within the rings (cf. Esposito *et al.*, 1983). However, Showalter and Nicholson (1986) present the following more plausible explanation, which does not invoke mysterious dynamical processes. The argument in favor of Poisson statistics neglects an additional source of scatter in the counts. One tends to think of the Saturnian ring system as a locally uniform, semitransparent screen, in which τ corresponds to the fraction of light which passes through. However, on distance scales comparable to the particle size this is clearly not the case; for geometric optics, the ring optical depth may only be infinity or zero, depending upon whether or not a ring particle interrupts the path of a photon. The effective ring area sampled by a single PPS bin is ~150 m long (in the reference frame of ring particles) and ~8 m wide (one Fresnel zone). In such a small area, the fractional area blocked by ~1-m ring particles will exhibit significant statistical scatter, even if the ring is uniform macroscopically. In effect, τ must be described by a probability distribution of its own. Showalter and Nicholson show that the curve (Fig. 4.1) may be explained by a ring particle size distribution which extends up to radii near 10 m; this is comparable to another estimate of the upper size limit in Saturn's rings, inferred from the radio occultation data (Marouf *et al.*, 1983). Note that the scatter should approach Poisson statistics in the limits $\bar{\tau} \rightarrow 0$ and $\bar{\tau} \rightarrow \infty$, where particle size is irrelevant.

For our purposes, we will use the results of the tabulation as an empirical model for the uncertainty in a given PPS count value, and weight each bin accordingly. Given the model and the weights, a nonlinear least-squares parameter fit determines the most plausible value for the moonlet's mass.

4.2. Data Analysis

Figure 4.2 shows the best fit mass values determined from fitting sections of the PPS scan's inner wake. The horizontal bars do not represent uncertainty, but rather the radial range of data used in each given mass estimate. For the most part, 200-bin sections of the data were used. The mass determinations are reasonably uniform until an abrupt dropoff appears at a radius of 133,380 km. This occurs 20 km before the abrupt phase shift in the scan, which we ascribed to the collective effects; apparently, these effects also act to reduce the overall amplitude of the wake, and therefore our naive mass estimate.

In this wake, no evidence for a significant variation in the background optical depth is found; thus, it is reasonable to perform a mass determination on a larger range of the

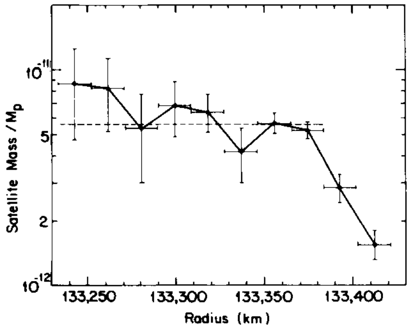

FIG. 4.2. The satellite's mass, as determined from sections of the inner PPS scan. The horizontal bars represent the radial segment of data going into each determination, and the vertical bar is the statistical uncertainty of the fit. The longer dashed line represents a single fit to a data segment eight times larger. The abrupt cutoff beyond 133,380 km is probably the result of collisions.

data. The long horizontal dashed bar in Fig. 4.2 represents a fit to 1600 PPS bins, which still excludes the section of the scan where collective effects seem to be at work. The mass is found to be $5.6 \pm 0.4 \times 10^{-12} M_p$. However, the small error quoted is merely the statistical uncertainty from the fit; any collisional damping of the wake amplitude, neglected in our model, would lead to an artificially small inferred mass. Figure 4.2 also reveals a slight upward trend in the mass determination with distance from the gap. Although this trend is not particularly significant in comparison with the uncertainty, it may indicate that some damping has occurred. For this reason, we regard $5 \times 10^{-12} M_p$ as a rigid lower limit on the moonlet's mass; a value perhaps twice as large cannot be excluded until collective effects are better understood. Nevertheless, according to Appendix A, we do not anticipate effects of this magnitude so close to the moonlet.

The same fitting procedure may be applied to the outer wake in the PPS scan, and its results are shown in Fig. 4.3. The mass determination appears to be considerably more erratic, which is probably a consequence of the greater evolution of this wake under collective effects. Nevertheless, we again see an abrupt breakpoint in the mass determination as the distance from the moonlet decreases (and streamline interactions become more important). The breakpoint occurs at a radius of 133,410 km, 30 km beyond the location of the abrupt phase shift in this scan. Again, the lack of a significant trend in τ_0 makes it possible to perform the fit over a larger range of data. The horizontal dashed line corresponds to a fit to 1200 PPS bins; it indicates a mass of $4.5 \pm 0.4 \times 10^{-12} M_p$, which is comparable to the previous estimate.

It would be desirable to derive the moonlet's mass from the radio scan as well as from the PPS. However, you will recall that when Σ is near unity (as is the case throughout this scan), only the optical depth maxima severely constrain the mass; the minima always approach a value of $\tau_0/2$. From Voyager's shallow viewing angle ($B = 5.9°$), the wake maxima are completely opaque to its radio transmissions. As a result, the radio scan is consistent with a broad range of moonlet mass values. Nevertheless, a few points may be made. First, the mere fact that the optical depth maxima appear opaque, even in the region of the profile most distant from the moonlet, indicates that $M_s \gtrsim 5 \times 10^{-12} M_p$. Furthermore, if M_s is much greater than $10 \times 10^{-12} M_p$ then streamlines would (naively) be ex-

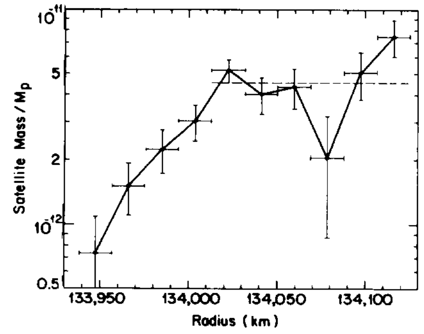

FIG. 4.3. The satellite's mass, as determined from the sections of the outer PPS scan. This plot is identical in meaning to Fig. 4.2.

pected to cross throughout the observed wake region; this may or may not be a serious constraint, since we do not well understand the effects of collisions. Nevertheless, the radio occultation seems to independently corroborate the mass range inferred from the PPS scan.

The mass of the Encke Gap moonlet almost definitely falls into the range 5–10 × $10^{-12} M_p$; the marginally smaller mass found from the outer PPS scan probably results from collisional damping. Assuming that it is composed primarily of water ice, the body has a radius of 9–10 km. This compares favorably with the mass estimated by CS (15 × $10^{-12} M_p$), based on the radial amplitude of the wavy edges. Any discrepancy may be ascribed to the difficulty in measuring such a small radial amplitude in the images, and also to the fact that the observed ripples must evolve under poorly understood collisional effects.

5. SUMMARY AND CONCLUSIONS

5.1. Summary of the Observations

We have shown that three different observed features near the Encke Gap in the PPS and radio scans all appear to be consistent with the gravitational wakes of a single hypothetical moonlet. These patterns complement the visual detection of wavy edges (CS). In Fig. 5.1, we graphically summarize the observations, and show how a single satellite may account for them all.

This satellite probably also accounts for the gap's existence, since its gravitational torques will act to "shepherd" away the surrounding ring material (cf. Lin and Papaloizou, 1979), in much the same way that two satellites Pandora and Prometheus are thought to confine the F Ring. This moonlet may also induce kinks and clumps in the Encke Gap's central ringlet, perhaps by processes similar to those at work in the F Ring; although this process is not understood, it may be more widespread than had been previously thought.

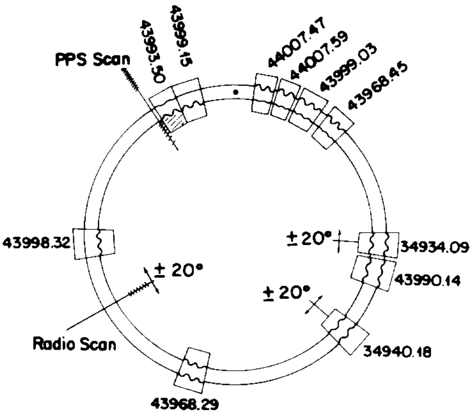

FIG. 5.1. A summary of all of the data now available on the Encke Gap moonlet, including the wavy edge images (CS; cf. their Fig. 7). Both scans are shown, and the sections containing visible wakes are noted with stripes. All of these observations may be accounted for by a single moon at the location shown by a solid circle.

As an additional piece of evidence for the moonlet, and as a visible illustration of the wake phenomenon, we call the reader's attention to the Voyager image designated FDS 43993.50 (see Fig. 5.1). This is the Encke Gap image with the best resolution (~5 km/pixel), and it falls rather close in longitude to the moonlet. This is also the frame in which Cuzzi first noted a wavy edge. By reprojecting and enhancing the contrast of this frame, the edge ripples become plainly visible (cf. CS, their Fig. 1). Using a slightly different contrast enhancement (Fig. 5.2), the nonazimuthal form of a density wake is also seen. At this short distance from the moonlet (26°), the wavelength is ~10 km (see Fig. 2.2b) and is therefore marginally resolved by the 5-km pixels. Although the wake is clearly visible it is too poorly resolved for a detailed analysis to further constrain the moonlet's orbit or mass.

5.2. Theoretical Implications

We have noted repeatedly that deviations of the data from our simple model are most probably caused by collective ring particle

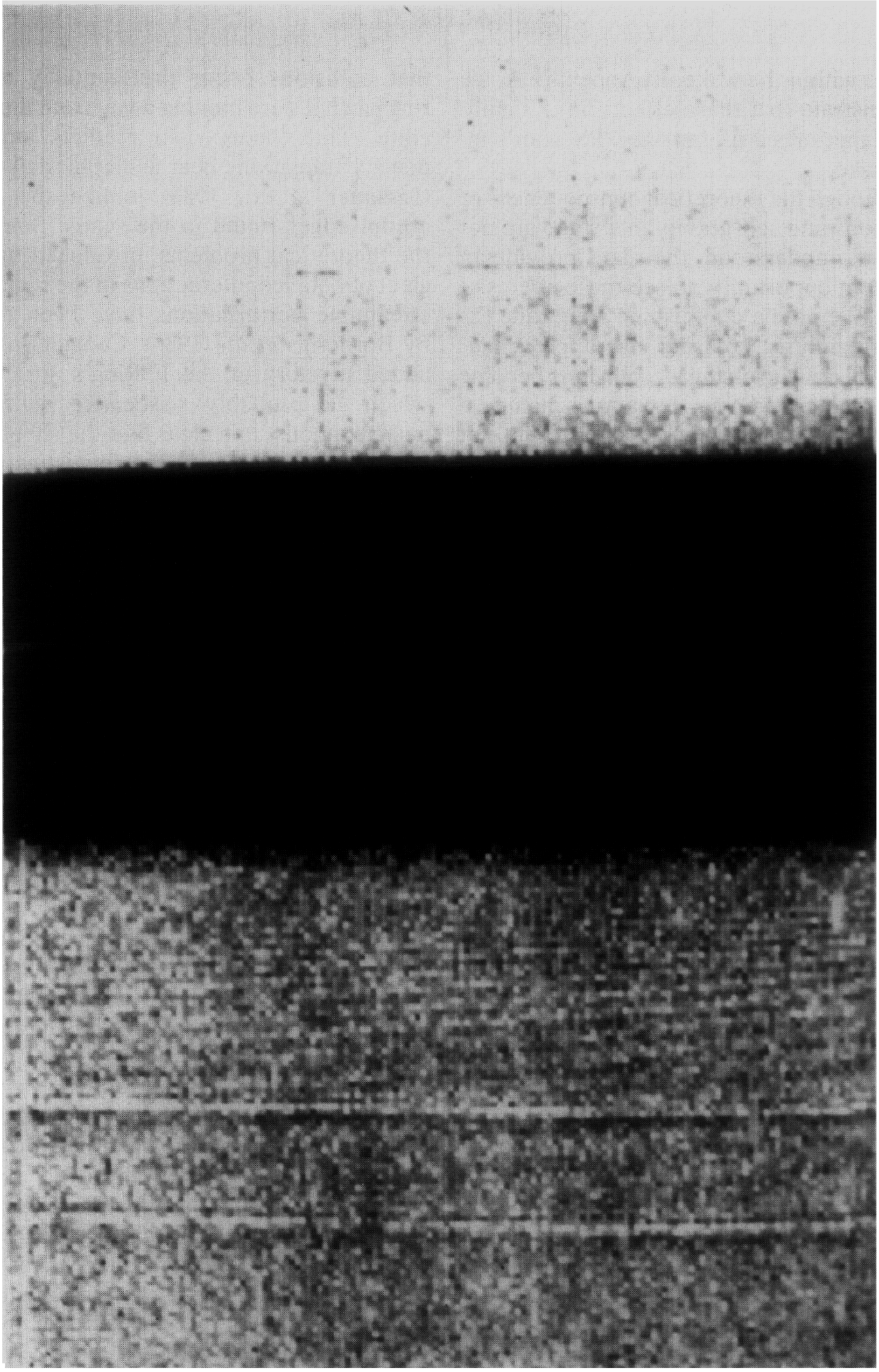

FIG. 5.2 Voyager 2 image FDS 43993.50, reprojected to remove overall curvature and to expand the radial scale. The narrow "kinky" ringlet is visible near the gap's center, and the inner (lower) edge shows distinct radial ripples. The Encke moonlet's wake is visible in the ring region inward from the gap, as a pattern of nonaximsymmetric stripes.

effects within the wake. In Appendix A, we demonstrate that these effects have significantly perturbed all but the PPS scan's inner wake.

Although the theoretical consequences of collisions and self-gravity in a wake are not currently understood, the scans provide an excellent opportunity to see these effects at work. We note a diminishing amplitude (Σ) as streamline crossing is approached, which is not surprising as collisions become more frequent. Other deviations include a radial wavelength which is altered (but not in a consistent direction) at large azimuthal distances, and the possible appearance of an abrupt phase shift where the amplitude is large. In a similar vein, Cuzzi and Scargle (1985) noted a persistence of the edge ripples far beyond the point where collisions should have damped them out; the edge wave appears to be self-reinforcing, and yet does not change significantly in azimuthal wavelength. The challenge of any full, self-consistent wake theory is to explain these observations.

However, such a theory would have considerably broader implications. The wake is essentially a short-term phenomenon from the standpoint of any particular ring particle; it receives a gravitational kick suddenly as the moonlet passes, is buffetted by collisions and self-gravity as the wake becomes more pronounced, and then settles into a relatively stable circular orbit until the moonlet's next encounter. However, the long-term sum of these gravitational kicks must be a "shepherding" of ring material away from the moonlet, and hence the clearing of a gap. The connection between these two effects is as yet not well understood. For example, the current shepherding theory estimates the flow of angular momentum by either summing over orbital resonances (Goldreich and Tremaine, 1980) or by using an impulse approximation which neglects the formation of a wake (Lin and Papaloizou, 1979). Both approaches ignore the systematics of particle collisions expected in a wake; it is clear from Fig. 1.2 that collisions occur preferentially when ring particles are moving away from the satellite. This theory also predicts smooth density transitions near a shepherded edge (Lissauer *et al.*, 1981), unlike the very abrupt edges found in the scans. Some of the theoretical problems introduced by neglect of detailed interactions in the region of streamline perturbations have been noted by Borderies *et al.* (1984). Considering the added mystery of the F Ring's structure, which is probably associated with its nearby moons, it is clear that the shepherding process requires further investigation.

With this caveat noted, it is interesting to compare the width of the Encke Gap with that expected from the moonlet's influence. The edges of the gap should fall where the torque due to viscous spreading of the ring material is precisely balanced by the torque of the moonlet. Based on our current understanding of the shepherding process (cf. CS, Sect. IVc), a body of the mass inferred could maintain a gap of 100–200 km radial width; this value is crudely comparable to the gap's observed 325 km width. An improved theory might indicate how a smaller moonlet could be responsible for the observed gap width.

Along with the work of Cuzzi and Scargle (1985), this paper has described the first detection of a moon embedded within an optically thick ring. It is not surprising that it should be associated with a new, previously unrecognized ring structure. For reasons given above, we believe that further theoretical study of the wake phenomenon will produce a greatly improved understanding of how the "shepherding" process actually works. In addition, the technique of detecting moonlets by their wakes may be of great use in future occultation studies of planetary rings by spacecraft or by the Hubble Space Telescope.

The Encke Gap moonlet, with a radius of about 10 km, is about the size of the moons of Mars. The presence of such a sizeable object residing well within Saturn's Roche limit has far-reaching implications for theories of the origin of Saturn's rings. The mere fact that the Encke moonlet is surrounded by ring material and not other moonlets attests to the disruptive effects of Saturn's tidal forces, which currently prevent ring bodies from accreting in this region. This situation probably has not changed over geologic time. Therefore, it is unlikely that the Encke Gap moonlet accreted at its present position; more likely, it accreted further from Saturn and evolved inward due to some primordial process, such as gas drag, which terminated before the moonlet was lost into the planet itself. One further possible inference is that neither did the ring material accrete in its current location; i.e., it is difficult to imagine an evolutionary process that could so strongly alter the orbit of a 10-km moon while leaving the orbits of far smaller bodies unaffected. This conclusion would become even stronger should moonlets of similar size be found within other gaps. Clearly, the processes which accompanied the formation of the Saturnian system were complex. An important constraint has now been added to our understanding of these processes.

APPENDIX A

COLLECTIVE EFFECTS

It is useful to estimate the importance of collisions and self-gravity, which were neglected in the analysis of Section 2, on the form of a moonlet wake. In particular, we wish to establish the magnitude and sign of possible errors in the moonlet's orbit, due to the neglect of these collective effects.

To obtain this estimate, we first include forces due to collisions and self-gravity in the equations of motion. We then make use of the nearly periodic local form of the final solutions for velocity and mass density to convert the linearized equations into a dispersion relation; this relates the wavenumber **k** to the distance from the moonlet, in terms of local mass density σ and dispersion velocity c. The difference between the wavenumber inferred in this manner from that found in the simple theory will indicate the role of collective effects. Because the dispersion relation is obtained from the linearized equations, it is quantitatively valid as long as $\Sigma \ll 1$. This condition is fulfilled for a substantial range of radii and longitudes, extending up to and including most of the region examined in the inner portion of the PPS scan. It is not, however, valid near the other scans of the Encke moonlet's wake. Our approach follows that of Hunter (1973).

We begin with the equations of continuity and motion, written in a frame rotating with the satellite at angular velocity ω_s:

$$\left(\frac{\partial}{\partial t} + \nabla \cdot \mathbf{v}\right) \sigma = 0, \qquad \text{(A.1a)}$$

$$\left(\frac{\partial}{\partial t} + (\mathbf{v} \cdot \nabla) + 2\boldsymbol{\omega}_s \times\right) \mathbf{v} + \boldsymbol{\omega}_s \times (\boldsymbol{\omega}_s \times \mathbf{r}) = \mathbf{f}, \qquad \text{(A.1b)}$$

where **f** is the perturbing acceleration (i.e., the force per unit ring mass). It may be expressed as

$$\mathbf{f} = -\nabla(\psi_p + \psi_d) - \frac{c^2}{\sigma_0}\nabla\sigma + \nu\nabla^2\mathbf{v}, \qquad \text{(A.2)}$$

with ψ_p the dominant gravitational potential due to the planet (including oblateness terms), and ψ_d the gravitational potential of the perturbed disk. The remaining terms describe collisions by forces due to pressure and viscosity, in which the coefficient of kinematic viscosity ν is approximated by

$$\nu \sim \frac{c^2}{2\omega}\frac{\tau}{1 + \tau^2} \qquad \text{(A.3)}$$

(Goldreich and Tremaine, 1978). We have omitted the additional bulk viscosity force from (A.2), as it leads to terms of the same form and order as the kinematic viscosity. We now linearize (A.1) by expanding σ and **v**:

$$\sigma = \sigma_0 + \sigma'(r, \theta, t), \qquad \text{(A.4a)}$$

$$v_r = u'(r, \theta, t), \qquad \text{(A.4b)}$$

$$v_\theta = r(\omega - \omega_s) + w'(r,\theta,t), \quad (A.4c)$$

where it is assumed that $|\sigma'| \ll \sigma_0$ and $|u', w'| \ll v_\theta$. In this regime, the equations of motion become (cf. Hunter, 1973)

$$\frac{\partial\sigma'}{\partial t} + (\omega - \omega_s)\frac{\partial\sigma'}{\partial\theta} + \frac{\sigma_0}{r}\frac{\partial(ru')}{\partial r} + \frac{\sigma_0}{r}\frac{\partial w'}{\partial\theta} = 0, \quad (A.5a)$$

$$\frac{\partial u'}{\partial t} + (\omega - \omega_s)\frac{\partial u'}{\partial\theta} - 2\omega w' = -\frac{\partial\psi_d}{\partial r} - \frac{c^2}{\sigma_0}\frac{\partial\sigma'}{\partial r} + \nu\nabla^2 u', \quad (A.5b)$$

$$\frac{\partial w'}{\partial t} + (\omega - \omega_s)\frac{\partial w'}{\partial\theta} + \frac{\kappa^2}{2\omega}u' = -\frac{1}{r}\frac{\partial\psi_d}{\partial\theta} - \frac{c^2}{\sigma_0 r}\frac{\partial\sigma'}{\partial\theta} + \nu\nabla^2[r(\omega - \omega_s) + w'], \quad (A.5c)$$

where we have used the standard relationship between epicyclic and orbital frequencies

$$\kappa^2 = 4\omega^2 + r\frac{d\omega^2}{dr}. \quad (A.6)$$

We now make use of our a priori knowledge of the solutions for u', w' and σ' (cf. eqs. 2.1.1 and 2.1.10), adopting for them the general wavelike form

$$X' = X_0 e^{i(k_r^* r + \eta^*\theta - \Omega t)}. \quad (A.7)$$

The star superscripts on the wavenumber components k_r^* and η^* indicate that these have been modified by collective forces, and therefore will differ slightly from values inferred in Section 2. In reality the quantities X_0, k_r^*, and η^* all vary slowly, but we assume that such variations are small on scales of a few wavelengths. Hence,

$$\frac{\partial X'}{\partial t} = -i\Omega X', \quad \frac{\partial X'}{\partial r} = ik_r^* X', \quad \frac{\partial X'}{\partial\theta} = i\eta^* X'. \quad (A.8)$$

The gravitational potential arising due to the (assumed) sinusoidal mass distribution is

$$\psi_d = -\frac{2\pi G\sigma'}{k^*} \approx -\frac{2\pi G\sigma'}{|k_r^*|} \quad (A.9)$$

The approximation $k^* \approx |k_r^*|$ is valid because most of the variations in a moonlet wake are radial; in other words $k_r^* \gg k_\theta^*$, where $k_\theta^* \equiv \eta^*/r$. Substituting (A.7)–(A.9) into (A.5) yields

$$W\sigma' - \sigma_0 k_r^* u' = 0, \quad (A.10a)$$

$$-\left(\frac{-2\pi G\sigma_0|k_r^*| + c^2k^{*2}}{k^*\sigma_0}\right)\sigma' + (W + i\nu_0 k^{*2})u' - (2i\omega)w' = 0, \quad (A.10b)$$

$$\left(\frac{i\kappa^2}{2\omega}\right)u' + (W + i\nu_0 k^{*2})w' = 0, \quad (A.10c)$$

where $W \equiv (\Omega - \eta^*(\omega - \omega_s))$, and ν_0 is the viscosity (A.3) evaluated at $\tau = \tau_0$. The variables u', w', and σ' may be readily eliminated, to yield the dispersion relation

$$\Omega = \eta^*(\omega - \omega_s) \pm [\kappa^2 - 2\pi G\sigma_0|k_r^*| + c^2k^{*2} + \nu_0^2 k^{*4}]^{1/2}. \quad (A.11)$$

It is necessary that $\Omega = 0$ for the solution to be steady in the rotating frame. This then determines the azimuthal wavenumber, with collective effects included, in terms of the total wavenumber $\mathbf{k}^*$ and average ring properties:

$$\eta^* = \frac{\kappa}{(\omega - \omega_s)}\left(1 - \frac{2\pi G\sigma_0|k_r^*|}{\kappa^2} + \frac{c^2k^{*2}}{\kappa^2} + \left(\frac{c^2k^{*2}}{2\kappa\omega}\frac{\tau_0}{1 + \tau_0^2}\right)^2\right)^{1/2}. \quad (A.12)$$

In the limit σ_0, $c \to 0$, η^* reduces to the form predicted by our simple theory (cf. 2.1.2). In the region between the stellar occultation and the moonlet, $\sigma_0 \approx 50$ g cm^{-2}, $c \approx 0.4$ cm sec^{-1} (Cuzzi *et al.*, 1984), $\tau_0 \approx 0.4$, and $k^* \approx k_r^* \lesssim 2\pi/5$ km. Thus the collective terms in parentheses in (A.12) are of order 10^{-2} (self-gravity), 10^{-3} (pressure), and 10^{-6} (viscosity), respectively. The viscosity term is comparable to the pressure term squared, and is excluded hereafter; its larger (first-order) effect is to damp the wake amplitude, but this does not appear in the real part of the dispersion relation. Since all the correction terms are small, we may safely substitute from (2.2.7) for k_r^* and k^*, obtaining

$$\eta^* = \eta\left(1 - \frac{2\pi G\sigma_0}{3a\kappa^2}\frac{|\theta|}{\delta^2} + \frac{2c^2}{9a^2\kappa^2}\frac{\theta^2}{\delta^4}\right), \quad (A.13)$$

or $\eta^* = \eta + \eta'(\theta)$, with η' representing a small wavenumber shift. We can now determine the value of θ for which collective effects become important at any level, and an approximate correction to our moonlet longitude.

As noted above, the larger term in the frequency correction is only of order 10^{-2} at the longitude of the PPS scan ($\theta = 32°$). However, even a small error in η can add up to significant error in angular distance to the moonlet if inferred from a distance of many waves downstream. Because a frequency shift is merely the derivative of a varying phase offset, we obtain the cumulative phase offset $\Delta\theta$ induced by neglect of collective effects:

$$\frac{\Delta\theta}{\lambda_\theta} = \frac{1}{2\pi}\int_0^\theta \eta'(\theta')d\theta'. \quad (A.14)$$

Substituting $\theta = 32°$ and other attributes of the Encke Gap region, we find that $\Delta\theta/\lambda_\theta$ ranges from 1–10% in the scan. This is comparable to the uncertainties in the data analysis, so that only small errors in the moonlet orbit arise from neglecting collective effects. The sign of $\Delta\theta$ is such that the moonlet is further away than inferred from the simple theory.

We can determine the modified radial wavelength due to collective effects from (A.13), by noting that $\lambda_r \propto (\partial\eta/\partial\delta)^{-1}$:

$$\lambda_r^* = \lambda_r\left(1 + \frac{2\pi G\sigma_0}{a\kappa^2}\frac{|\theta|}{\delta^2} - \frac{10c^2}{9a^2\kappa^2}\frac{\theta^2}{\delta^4}\right). \quad (A.15)$$

Thus, the initial effect of self-gravity is to increase λ_r. This is opposite to the observed effect in the radio scan, in which the wavelength is reduced by ~20%. However, it should be noted that the pressure term in (A.15) increases more rapidly with θ, and dominates at the gap edge beyond $\theta \approx 130°$ (if we may extrapolate into this regime). Intuitively, one certainly expects collisions to dominate near streamline crossing. This term is also opposite in sign to the self-gravity effect, and has an amplitude of 10–20% at the gap edge in the radio scan. Although the pressure effects will be reduced inward from the edge, they seem roughly consistent with the observations. Aside from these qualitative results, however, a linearized theory is inadequate to describe this scan. We are currently exploring a more satisfactory treatment of this interesting (but distinctly nonlinear) situation.

APPENDIX B

ANGULAR REFERENCE FRAMES

The Voyager 1 radio occultation and the Voyager 2 stellar occultation data sets are generally referenced to different coordinate frames. In this appendix, we note the method of relating these frames to our primary reference frame: Earth's mean equator and Vernal equinox of 1950 (EME50).

Longitudes along the radio occultation track are given by the experimenters as angles measured counterclockwise (i.e., eastward) from the ring plane ascending node on the Earth's mean equator, $\mathbf{\Omega}$. Longitudes on the stellar occultation track are measured clockwise (west) from the subsolar direction at the time of the Voyager 1 encounter, $\mathbf{S}_{\mathrm{V1}}$, projected into the ring

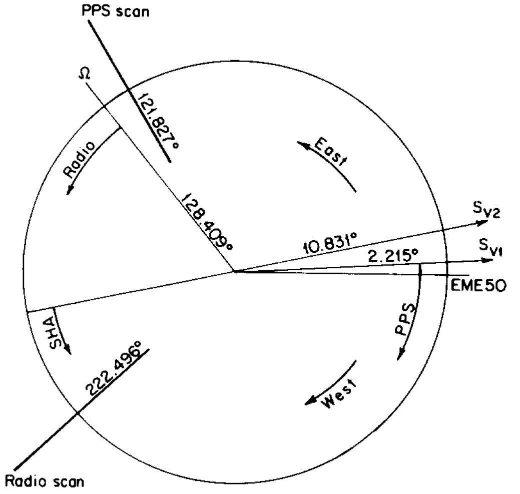

FIG. B.1. A view of the relevant origin vectors of alternative angular coordinate frames, as projected into the Saturn ring plane. The view is from directly above the north pole, with the EME50 reference direction toward the right. The locations is inertial space of the stellar and radio occultations are also shown.

plane. An additional frame, used by CS, is the solar hour angle (SHA) system, measured eastward along the ring plane from the antisolar direction ($-\mathbf{S}_{V1}$ or $-\mathbf{S}_{V2}$) at the epoch of the Voyager 1 or 2 encounters. In this paper we give all of our results in the more standard EME50 system, in which longitudes are measured eastward along the Earth's equator to the ring plane ascending node, and thence along the ring plane.

The key to converting between these frames is the Saturn pole vector $\mathbf{Z}$, which is perpendicular to the ring plane. It has been most accurately determined by Simpson *et al.* (1983) by comparing the geometries of the radio and stellar occultations: $\alpha_{1950} = 38.409°$, $\delta_{1950} = 83.324°$. J. Holberg (private communication, 1985) has provided accurate subsolar directions: for V1, $\alpha = 2.030°$ and $\delta = -5.380°$; for V2, $\alpha = 10.670°$ and $\delta = -5.914°$. Figure B.1 summarizes the directions of the relevant vectors in inertial space, as projected into the ring plane. Our reference longitude for the PPS scan is given by Holberg as 190.388° west of $\mathbf{S}_{V1}$, which places it at 121.827° in EME50; the reference longitude for the radio scan is 94.087° east of the ascending node, or 222.496° in EME50.

ACKNOWLEDGMENTS

We are grateful to Tony Ferro, Amara Graps and Jay Holberg for assistance with the data analysis, and to Joe Burns, Stan Dermott, Jack Lissauer, Phil Nicholson, Frank Shu and Len Tyler for helpful discussions and comments. MRS was supported in part by NASA Grant NAGW-310.

REFERENCES

BORDERIES, N., P. GOLDREICH, AND S. TREMAINE (1984). Unsolved problems in planetary ring dynamics. In *Planetary Rings* (R. Greenberg and A. Brahic, Eds.), pp. 713–734. Univ. of Arizona Press, Tucson.

CUZZI, J. N., J. J. LISSAUER, L. W. ESPOSITO, J. B. HOLBERG, E. A. MAROUF, G. L. TYLER, AND A. BOISCHOT (1984). Saturn's rings: Properties and processes. In *Planetary Rings* (R. Greenberg and A. Brahic, Eds.), pp. 73–199. Univ. of Arizona Press, Tucson.

CUZZI, J. N., AND J. D. SCARGLE (1985). Wavy edges suggest moonlet in Encke's Gap. *Astrophys. J.* **292,** 276–290.

DERMOTT, S. J. (1981). The 'braided' F Ring of Saturn. *Nature* **290,** 454–457.

ESPOSITO, L. W., M. O'CALLAGHAN, AND R. A. WEST (1983). The structure of Saturn's rings: Implications from the Voyager stellar occultation. *Icarus* **56,** 439–452.

GOLDREICH, P., AND S. TREMAINE (1978). The velocity dispersion in Saturn's rings. *Icarus* **34,** 227–239.

GOLDREICH, P., AND S. TREMAINE (1980). Disk-satellite interactions. *Astrophys. J.* **241,** 425–441.

GREENBERG, R. (1981). Apsidal precession of orbits about an oblate planet. *Astron. J.* **86,** 912–914.

HÉNON, M. (1981). A simple model of Saturn's rings. *Nature* **293,** 33–35.

HÉNON, M. (1983). A simple model of Saturn's rings—revisited. In *Planetary Rings* (A. Brahic, Ed.), pp. 363–384. CNES, Toulouse, France.

HUNTER, C. (1973). Patterns of waves in galactic disks. *Astrophys. J.* **181,** 685–705.

JULIAN, W., AND A. TOOMRE (1966). Non-axisymmetric responses of differentially rotating disks of stars. *Astrophys. J.* **146,** 810–830.

LANE, A. L., C. W. HORD, R. A. WEST, L. W. ESPOSITO, D. L. COFFEEN, M. SATO, K. E. SIMMONS, R. B. POMPHREY, AND R. B. MORRIS (1982). Photopolarimetry from Voyager 2: Preliminary results on Saturn, Titan and the rings. *Science* **215,** 537–553.

LIN, C. C., AND J. PAPALOIZOU (1979). Tidal torques on accretion disks in binary systems with extreme mass ratios. *Mon. Not. R. Astron. Soc.* **186,** 799–812.

LISSAUER, J. J., AND J. N. CUZZI (1982). Resonances in Saturn's rings. *Astron. J.* **87,** 1051–1058.

LISSAUER, J. J., F. H. SHU, AND J. N. CUZZI (1981). Moonlets in Saturn's rings? *Nature* **292,** 707–711.

MAROUF, E. A., G. L. TYLER, AND V. R. ESHLEMAN (1982). Theory of radio occultation by Saturn's rings. *Icarus* **49,** 161–193.

MAROUF, E. A., G. L. TYLER, AND P. A. ROSEN (1986). *Profiling Saturn's Rings by Radio Occultation.* Submitted for publication.

MAROUF, E. A., G. L. TYLER, H. A. ZEBKER, R. A. SIMPSON, AND V. R. ESHLEMAN (1983). Particle size distributions in Saturn's rings from Voyager 1 radio occultation. *Icarus* **54,** 189–211.

NULL, G. W., E. L. LAU, E. D. BILLER, AND J. D. ANDERSON (1981). Saturn gravity results obtained from Pioneer 11 tracking data and Earth-based Saturn satellite data. *Astron. J.* **86,** 456–468.

SHOWALTER, M. R. (1984). Effects of shepherd conjunctions on Saturn's F ring. In *Planetary Rings* (A. Brahic, Ed.), pp. 423–429. CNES, Toulouse, France.

SHOWALTER, M. R., AND J. A. BURNS (1982). A numerical study of Saturn's F ring. *Icarus* **52,** 526–544.

SHOWALTER, M. R., AND P. D. NICHOLSON (1986). *Statistical Scatter in the PPS Scan: Constraints on Particle Sizes in Saturn's Rings.* In preparation.

SHU, F. H., L. DONES, J. J. LISSAUER, C. YUAN, AND J. N. CUZZI (1985). Nonlinear spiral density waves: Viscous damping. *Astrophys. J.*, in press.

SIMPSON, R. A., G. L. TYLER, AND J. B. HOLBERG (1983). Saturn's pole: Geometric correction based on Voyager UVS and radio occultations. *Astron. J.* **88,** 1531–1536.

SMITH, B. A., L. SODERBLOM, R. BATSON, P. BRIDGES, J. INGE, H. MASURSKY, E. SHOEMAKER, R. BEEBE, J. BOYCE, G. BRIGGS, A. BUNKER, S. A. COLLINS, C. J. HANSEN, T. V. JOHNSON, J. L. MITCHELL, R. J. TERRILE, A. F. COOK II, J. CUZZI, J. B. POLLACK, G. E. DANIELSON, A. P. INGERSOLL, M. E. DAVIES, G. E. HUNT, D. MORRISON, T. OWEN, C. SAGAN, J. VEVERKA, R. STROM, AND V. E. SUOMI (1982). A new look at the Saturn system: The Voyager images. *Science* **215,** 504–537.

SMITH, B. A., L. SODERBLOM, R. BEEBE, J. BOYCE, G. BRIGGS, A. BUNKER, S. A. COLLINS, C. J. HANSEN, T. V. JOHNSON, J. L. MITCHELL, R. J. TERRILE, M. CARR, A. F. COOK II, J. CUZZI, J. B. POLLACK, G. E. DANIELSON, A. INGERSOLL, M. E. DAVIES, G. E. HUNT, H. MAZURSKY, E. SHOEMAKER, D. MORRISON, T. OWEN, C. SAGAN, J. VEVERKA, R. STROM, AND V. E. SUOMI (1981). Encounter with Saturn: Voyager 1 imaging science results. *Science* **212,** 163–191.

TYLER, G. L., V. R. ESHLEMAN, J. D. ANDERSON, G. S. LEVY, G. F. LINDAL, G. E. WOOD, AND T. A. CROFT (1981). Radio science investigations of the Saturn system with Voyager 1: Preliminary results. *Science* **212,** 201–206.

TYLER, G. L., E. A. MAROUF, R. A. SIMPSON, H. A. ZEBKER, AND V. R. ESHLEMAN (1983). The microwave opacity of Saturn's rings at wavelengths of 3.6 and 13 cm from Voyager 1 radio occultation. *Icarus* **54,** 160–188.